Iraqi Journal of Physics, 2025 *Vol.23, No.3, PP.50-65*
https://doi.org/10.30723/ijp.v23i3.1365 *P-ISSN: 2070-4003*
E-ISSN: 2664-5548

Role of Tin Oxide on the Structural, Optical and Electrical Properties of Pulsed Laser Deposited $(ZnO)_{1-x}(SnO_2)_x$ Composite Thin Films

Laith Kh. Ibraheem[1*] and Bushra A. Hasan[1]
[1]*Department of Physics, College of Science, University of Baghdad, Baghdad, Iraq*
[*]Corresponding author: laith.ibrahim2304@sc.uobaghdad.edu.iq

Abstract

This research examines the electrical, optical, and structural properties of zinc oxide (ZnO) and tin(IV) oxide $(ZnO)_{1-x}$ $(SnO_2)_x$ composite thin films made by pulsed laser deposition, as well as the impact of composition concentration. The structural study of $(ZnO)_{1-x}$ $(SnO_2)_x$ composites and thin films was conducted by X-ray analysis (XRD). Optical properties were investigated by UV–Vis infrared spectroscopy. The structural analysis revealed that all prepared thin-film composites were polycrystalline, exhibiting both hexagonal wurtzite and tetragonal phases for pure ZnO and SnO_2, as well as a mixture of both phases for x=0.2 and 0.4. In contrast, the SnO2 phase was predominant for x=0.6 and 0.8. The increase in crystal size in the $(ZnO)_{1-x}$ $(SnO_2)_x$ composite thin films was observed at x = 0.4 and 1.0. The optical band gap of $(ZnO)_{1-x}$ $(SnO_2)_x$ composites exhibited a distinct trend as the concentration of tin oxide increased. The average optical transmission ranges from 33% to 65% in the visible region. The maximum electrical conductivity of 1.13×10^2 $(\Omega cm)^{-1}$ was obtained in the film $(ZnO)_{0.8}$ $(SnO_2)_{0.2}$. Based on our findings, thin-film solar cells and touchpad control panels could benefit from $(ZnO)_{1-x}$ $(SnO_2)_x$ composite films due to their enhanced electrical and optical properties.

Article Info.

Keywords:
Thin Film, Tin Dioxide (SnO_2), Zinc Oxide (ZnO), PLD, Optical and Structural Properties.

Article history:
Received: Sep. 06, 2024
Revised: Jan. 04, 2025
Accepted: Jan. 11, 2025
Published:Sep. 01, 2025

1. Introduction

Since they have many intriguing applications in photovoltaic applications, catalysis, gas sensing, antistatic coating, and transparent conducting oxides as solar electrodes, a large number of pristine, doped, or composite materials based on zinc and/or tin oxide have been thoroughly studied in various morphologies over the past few decades [1-15]. Because Transparent Conducting Oxide (TCO) films have the ideal blend of high electrical conductivity and good optical transparency, they are frequently utilized in optoelectronic devices, including solar cells, thin film transistors, infrared (IR) reflectors, transparent electrodes, and flat panel displays[16-19]. Over the past 50 years, a number of binary compounds have been investigated as possible TCO candidates, including Indium (III) oxide (In_2O_3), zinc oxide (ZnO), and tin oxide (SnO_2). With a huge exciton energy of 60 MeV, ZnO is an n-type semiconductor with a wide band gap 3.37 eV at ambient temperature. However, ZnO's vulnerability to corrosion in very acidic and alkaline environments is a serious disadvantage. However, pure SnO_2, a semiconductor with a wide band gap 3.6 eV, does not meet industrial standards for clear conducting electrodes used in the production of solar cells. Both donor and acceptor doped and/or composite metal oxide semiconductors were extensively studied in an attempt to address this issue. When doped with F, SnO_2 exhibits conductivities of up to 9000 S/cm, making it the most often used TCO for low emissivity coatings on architectural glass [20]. Minami et al. [21] initially claimed that the benefits of both ZnO and SnO_2 may be combined in SnO_2–ZnO binary oxides. In spite of challenges in chemical etching, especially at greater concentrations of metallic Sn, SnO_2–ZnO composite films could replace the current TCO in some uses. Since Zn and Sn are more plentiful than indium, SnO_2–ZnO composite sheets can become a reasonably cheap substitute. The two materials have the combined

benefit of ZnO better stability under decreasing environment and SnO_2 outstanding thermal stability and mechanical strength. It is important to underline that many factors affect the performance and efficiency of the TCO: dopant concentration, deposition circumstances, and annealing technique. Many of the TCO thin films have been effectively produced in past years with the Pulsed Laser Deposition (PLD) method. Though uniformity across a vast area is a big issue, it has several advantages as opposed to other deposition processes, including accuracy of thickness, shape and desired composition of the films produced out of multi-component targets. Since the kinetic energy >1 eV of the ionized and ejected species created by the laser plasma is always greater, the substrate temperatures of the PLD films can be quite lower than those of conventional PVD processes. In this study, structural, optical, and electrical characteristics of $(ZnO)_{1-x}$ $(SnO_2)_x$ composites formed by PLD on glass substrate with varying SnO_2 levels were investigated. To the best of our knowledge, this is the preliminary work to employ PLD to generate binary thin films of $(ZnO)_{1-x}$ $(SnO_2)_x$ composites for the creation of TCO coatings or devices.

2. Experimental Work

ZnO and SnO_2 oxides used in this research supplied by Sigma-Aldrich company were used to prepare the $(ZnO)_{1-x}$ (SnO_2)x compounds. This was accomplished using the proper mass of high purity 99.99% of zinc and tin oxide powders supplied in different ratios x=0, 0.2, 0.4, 0.6, 0.8 and 1.0 that were weighed using an electronic balance. A quartz ampoule of 25 cm in length and 8 mm in internal diameter was used to heat the material to 1273 K and then leave it there for one hour in order to sinster it. The material was then homogenized by grinding it. The powder was shaped into pelts. A disk of one centimeter in diameter and half a centimeter in thickness was hammered into it. The following settings were selected for the deposition of high-quality and uniform films using a Nd:YAG laser beam: laser energy = 500 mJ, base pressure = 2×10^{-2} mbar, substrate-to-target distance = 45 mm, repetition rate = 6 Hz, and laser shots = up to 200. The film thickness (t) was measured using the optical interferometer technique. With a He-Ne laser set to 632.8 nm, this technique relies on the interference of light beams reflected from the substrate bottom and the thin film surface. The thickness was calculated using the formula

$$t = \frac{\lambda}{2}\frac{\Delta x}{x} \qquad (\mathbf{1})$$

where Δx, and x are the fringe width and the distance between the interference fringes, respectively, and λ is the He:Ne laser wavelength 632.8 nm. The crystal structure and crystallinity of $(ZnO)_{1-x}$ $(SnO_2)_x$ composite and the prepared thin films were measured by XRD using CuKα radiation (λ = 1.5406Å). An optical spectrophotometer (Shimadzu, UV-180, Japan) was used to perform the measurements. Using the Scherer formula

$$\mathrm{D} = \frac{0.9\lambda}{\beta\cos\theta} \qquad (\mathbf{2})$$

The average crystallite size (D) was determined. The formula takes into account the X-ray wavelength (λ), the Bragg diffraction angle (θ), and the full width at half maximum (FWHM) of the XRD peak that appears at diffraction angle θ [22].

The prepared $(ZnO)_{1-x}(SnO_2)_x$ thin film absorbance and transmittance spectra were measured using the device's wavelengths, which ranged from 190 to 1100 nm. The equation that follows was used to determine the absorption coefficient (α)

$$\alpha = \frac{2.303A}{t} \quad (3)$$

where t is the thin film thickness, and A is the absorbance. For direct allowed transitions, Tauc relation was utilized to estimate the optical energy gap (E_g) [23]

$$\alpha h\nu = \beta \left(h\nu - E_g\right)^r \quad (4)$$

where B is a constant. The following equations were used to measure the optical constants, real and imaginary dielectric constants, extinction coefficient, and refractive index

$$k = \frac{\alpha\lambda}{4\pi} \quad (5)$$

$$n = \sqrt{\frac{4R}{(R-1)^2} - k^2} - \frac{(R+1)}{(R-1)} \quad (6)$$

$$R = \frac{(n-1)^2 + k^2}{(n+1)^2 + k^2} \quad (7)$$

$$\varepsilon_r = n^2 - k^2 \quad (8)$$

$$\varepsilon_i = 2nk \quad (9)$$

3. Results and Discussion

3.1 XRD Spectra Analysis

The XRD patterns of the fabricated $(ZnO)_{1-x}$ $(SnO_2)_x$ composites are displayed in Fig. 1. From the diffraction pattern, it was seen that the crystallinity of the deposited films improved significantly at x=0.8. The XRD pattern of pure ZnO shows characteristic peaks that match the hexagonal phase of quartzite ZnO. The presence of peaks related to tetragonal rutile phase of SnO_2 (in addition to hexagonal ZnO) confirms the formation of the composites of ZnO and SnO_2. No other peaks were observed, which proved that the $ZnO)_{1-x}$ $(SnO_2)_x$ composite was formed with relatively high crystal purity. The XRD pattern for pure SnO_2 (x=1.0) was shown, which confirms the presence of characteristic peak of SnO_2 without any impurity. It can be observed that the intensity of the main diffraction peak for SnO_2 increased by increasing its concentration reaching maximum height at x=1.0.

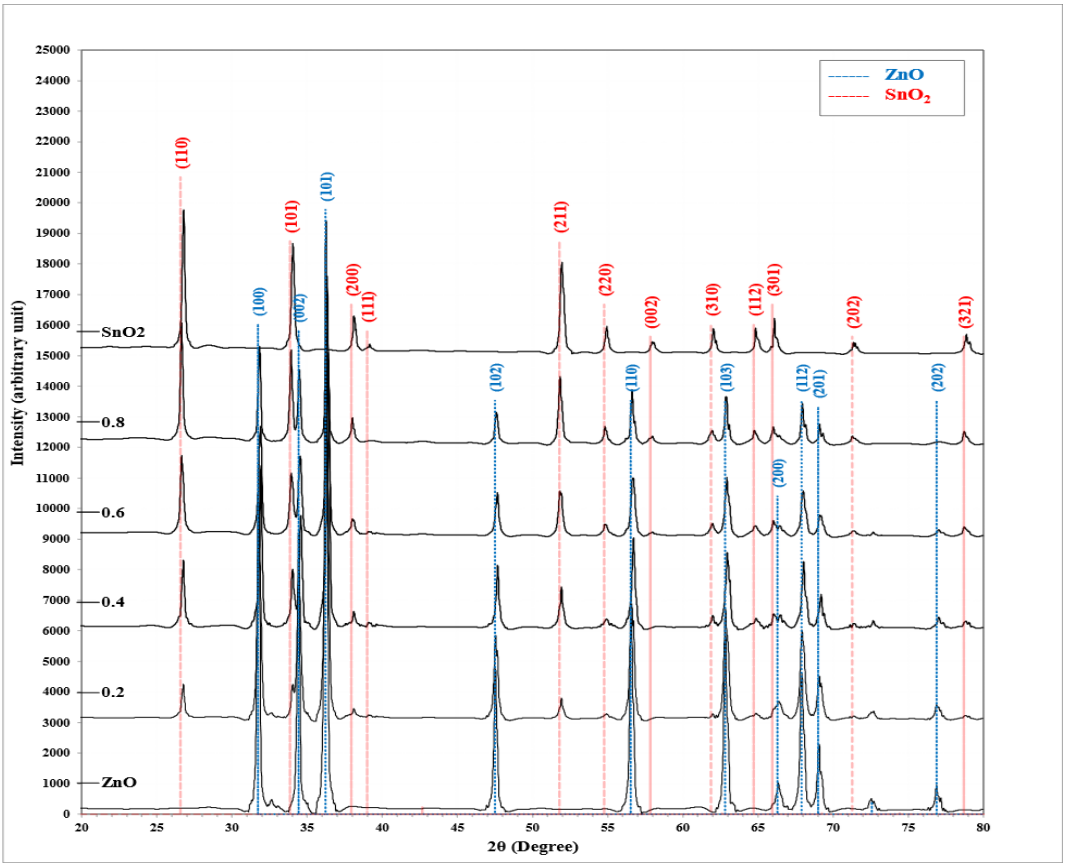

Figure 1: The XRD patterns of $(ZnO)_{1-x}$ $(SnO_2)_x$ nanocomposite produced by solid state reaction.

Table 1:The x-ray diffraction data of $ZnO)_{1-x}$ $(SnO_2)_x$ nanocomposite.

Sample	2θ (Deg.)	FWHM (Deg.)	d_{hkl} Exp.(Å)	G.S (nm)	Phase	hkl	card No.
ZnO	31.7650	0.2271	2.8148	36.4	ZnO	(100)	96-900-4182
	34.4358	0.2136	2.6023	38.9	ZnO	(002)	96-900-4182
	36.2653	0.2537	2.4751	33.0	ZnO	(101)	96-900-4182
	47.5362	0.2804	1.9112	31.0	ZnO	(102)	96-900-4182
	56.5769	0.3205	1.6254	28.1	ZnO	(110)	96-900-4182
	62.8533	0.3605	1.4773	25.8	ZnO	(103)	96-900-4182
	66.3521	0.3339	1.4077	28.4	ZnO	(200)	96-900-4182
	67.9279	0.3740	1.3788	25.6	ZnO	(112)	96-900-4182
	69.0630	0.3339	1.3589	28.9	ZnO	(201)	96-900-4182
	76.8751	0.4006	1.2391	25.3	ZnO	(202)	96-900-4182
x=0.2	26.7463	0.2472	3.3304	33.0	SnO_2	(110)	96-900-9083
	31.9357	0.3460	2.8001	23.9	ZnO	(100)	96-900-4182
	34.4069	0.2471	2.6044	33.7	ZnO	(002)	96-900-4182
	36.2850	0.2224	2.4738	37.6	ZnO	(101)	96-900-4182
	47.5288	0.3459	1.9115	25.1	ZnO	(102)	96-900-4182
	51.9028	0.2472	1.7602	35.7	SnO_2	(211)	96-900-9083
	56.5980	0.3706	1.6249	24.3	ZnO	(110)	96-900-4182
	62.8501	0.3707	1.4774	25.1	SnO_2	(310)	96-900-9083
	66.3839	0.4696	1.4071	20.2	SnO_2	(301)	96-900-9083
	67.9407	0.3460	1.3786	27.7	ZnO	(112)	96-900-4182
	69.1021	0.3459	1.3582	27.9	ZnO	(201)	96-900-4182
	76.9605	0.4201	1.2379	24.2	ZnO	(202)	96-900-4182
x=0.4	26.7705	0.2404	3.3275	34.0	SnO_2	(110)	96-900-9083
	31.9252	0.2403	2.8010	34.4	ZnO	(100)	96-900-4182

	34.0352	0.2271	2.6320	36.6	SnO_2	(101)	96-900-9083
	34.5960	0.2137	2.5906	38.9	ZnO	(002)	96-900-4182
	36.3855	0.2270	2.4672	36.8	ZnO	(101)	96-900-4182
	38.0948	0.1736	2.3603	48.4	SnO_2	(211)	96-900-9083
	47.6831	0.2137	1.9057	40.6	ZnO	(110)	96-900-4182
	51.9430	0.2671	1.7590	33.1	SnO_2	(310)	96-900-9083
	56.7238	0.2404	1.6216	37.6	ZnO	(110)	96-900-4182
	61.9987	0.1736	1.4956	53.4	ZnO	(103)	96-900-4182
	62.9602	0.3472	1.4751	26.8	SnO_2	(310)	96-900-9083
	66.0183	0.2671	1.4140	35.5	SnO_2	(301)	96-900-9083
	68.0481	0.2538	1.3767	37.8	ZnO	(112)	96-900-4182
	69.1965	0.2137	1.3566	45.2	ZnO	(201)	96-900-4182
	77.0220	0.2003	1.2371	50.7	ZnO	(202)	96-900-4182
x=0.6	26.6503	0.2537	3.3422	32.2	SnO_2	(110)	96-900-9083
	31.8985	0.2670	2.8033	30.9	ZnO	(100)	96-900-4182
	33.9550	0.2270	2.6380	36.6	SnO_2	(101)	96-900-9083
	34.5293	0.2271	2.5955	36.6	ZnO	(002)	96-900-4182
	36.3187	0.2805	2.4716	29.8	ZnO	(101)	96-900-4182
	38.0548	0.2003	2.3627	42.0	SnO_2	(211)	96-900-9083
	47.6564	0.2403	1.9067	36.1	ZnO	(110)	96-900-4182
	51.8362	0.2937	1.7624	30.1	SnO_2	(310)	96-900-9083
	54.8275	0.2271	1.6731	39.4	SnO_2	(220)	96-900-9083
	56.6837	0.2938	1.6226	30.7	ZnO	(110)	96-900-4182
	61.9452	0.2804	1.4968	33.0	ZnO	(103)	96-900-4182
	62.9335	0.3071	1.4757	30.3	SnO_2	(310)	96-900-9083
	64.8431	0.3072	1.4367	30.6	SnO_2	(112)	96-900-9083
	66.0049	0.2404	1.4142	39.4	SnO_2	(301)	96-900-9083
	68.0080	0.3339	1.3774	28.7	ZnO	(112)	96-900-4182
	69.1431	0.2537	1.3575	38.0	ZnO	(201)	96-900-4182
	78.7314	0.2270	1.2145	45.3	SnO_2	(321)	96-900-9083
x=0.8	26.6503	0.1870	3.3422	43.7	SnO_2	(110)	96-900-9083
	31.8184	0.2003	2.8101	41.2	ZnO	(100)	96-900-4182
	33.9417	0.2003	2.6391	41.5	SnO_2	(101)	96-900-9083
	34.4892	0.1870	2.5984	44.5	ZnO	(002)	96-900-4182
	36.3187	0.2538	2.4716	32.9	ZnO	(101)	96-900-4182
	38.0280	0.2136	2.3643	39.3	SnO_2	(211)	96-900-9083
	47.6029	0.2270	1.9087	38.3	ZnO	(110)	96-900-4182
	51.8362	0.2804	1.7624	31.5	SnO_2	(310)	96-900-9083
	54.8142	0.2270	1.6734	39.4	SnO_2	(220)	96-900-9083
	56.6437	0.2003	1.6237	45.1	ZnO	(110)	96-900-4182
	57.8856	0.2938	1.5917	30.9	SnO_2	(002)	96-900-9083
	61.9185	0.3205	1.4974	28.9	ZnO	(103)	96-900-4182
	62.8800	0.1736	1.4768	53.6	SnO_2	(310)	96-900-9083
	64.7630	0.2404	1.4383	39.1	SnO_2	(112)	96-900-9083
	66.0316	0.2804	1.4137	33.8	SnO_2	(301)	96-900-9083
	67.9680	0.1870	1.3781	51.2	ZnO	(112)	96-900-4182
	69.1164	0.1335	1.3580	72.3	ZnO	(201)	96-900-4182
	71.2931	0.1869	1.3218	52.3	SnO_2	(202)	96-900-9083
	78.7047	0.2270	1.2148	45.3	SnO_2	(321)	96-900-9083
	26.7839	0.2003	3.3258	40.8	SnO_2	(110)	96-900-9083
SnO_2	34.0485	0.2270	2.6310	36.6	SnO_2	(101)	96-900-9083
	38.1349	0.2403	2.3580	35.0	SnO_2	(211)	96-900-9083
	39.1498	0.1602	2.2991	52.6	SnO_2	(111)	96-900-9083
	51.9430	0.2938	1.7590	30.1	SnO_2	(310)	96-900-9083

	54.9343	0.1869	1.6701	47.9	SnO_2	(220)	96-900-9083
	57.9791	0.2805	1.5894	32.4	SnO_2	(002)	96-900-9083
	62.0254	0.2004	1.4951	46.3	SnO_2	(310)	96-900-9083
	64.8564	0.1736	1.4365	54.2	SnO_2	(112)	96-900-9083
	66.0984	0.1736	1.4125	54.6	SnO_2	(301)	96-900-9083
	71.3599	0.2404	1.3207	40.7	SnO_2	(202)	96-900-9083
	78.8783	0.2404	1.2126	42.8	SnO_2	(321)	96-900-9083

The XRD patterns of $(ZnO)_{1-x}$ $(SnO_2)_x$ nanocomposite thin films of ~150 nm thickness created by the pulsed laser method at room temperature are displayed in Fig. 2. Thin film composition rates were from x=0 to 1%. Eight diffraction peaks located at 2θ = 31.74°, 34.4°, 36.24°, 47.54°, 56. 58°, 62.85°, 67.92° and 69.06° corresponding to the planes (100), (002), (101), (102), (110), (103) and (112) and (201), respectively, of ZnO. Four major diffraction peaks at 2θ = 26.6°, 33.86°, 37.93° and 51.73° can be assigned to the planes (110), (101), (200), and (211), respectively of SnO_2.

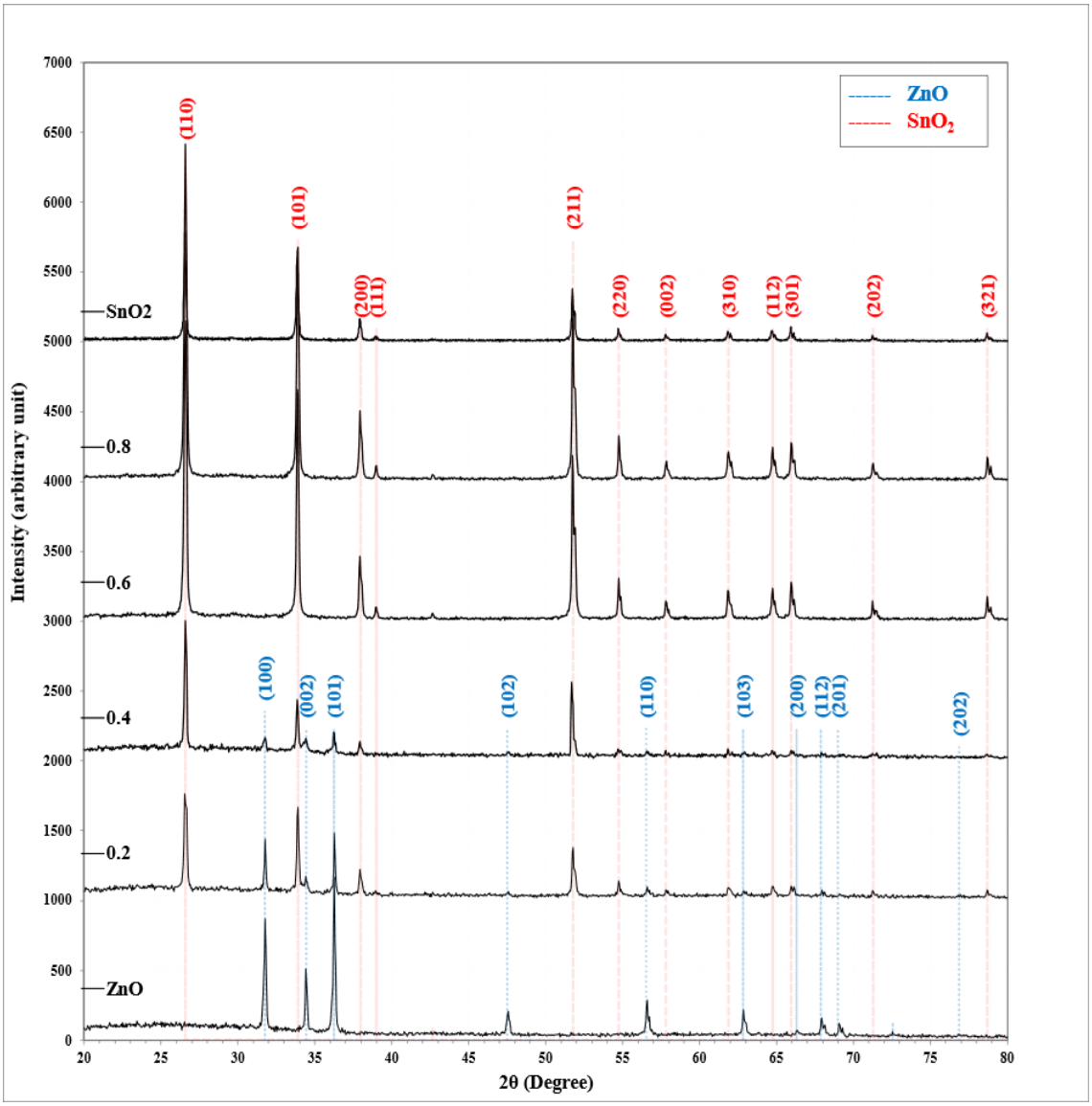

Figure 2: XRD patterns of $(ZnO)_{1-x}$ $(SnO_2)_x$ nanocomposite thin films.

Table 2: The diffraction of x-rays data for $(ZnO)_{1-x}$ $(SnO_2)_x$ nanocomposite thin films.

Sample	2θ (Deg.)	FWHM (Deg.)	d_{hkl} Exp.(Å)	G.S (nm)	Phase	hkl	card No.
ZnO	31.7424	0.1840	2.8167	44.9	ZnO	(100)	96-900-4182
	34.4020	0.2007	2.6048	41.4	ZnO	(002)	96-900-4182
	36.2420	0.1840	2.4767	45.4	ZnO	(101)	96-900-4182
	47.5495	0.2175	1.9107	39.9	ZnO	(102)	96-900-4182
	56.5821	0.2677	1.6253	33.7	ZnO	(110)	96-900-4182
	62.8548	0.2510	1.4773	37.1	ZnO	(103)	96-900-4182
	67.9231	0.2676	1.3789	35.8	ZnO	(112)	96-900-4182
	69.0605	0.2342	1.3589	41.2	ZnO	(201)	96-900-4182
x=0.2	26.5570	0.2007	3.3537	40.7	SnO_2	(110)	96-900-9083
	31.7424	0.1338	2.8167	61.7	ZnO	(100)	96-900-4182
	33.8667	0.2007	2.6447	41.4	SnO_2	(101)	96-900-9083
	34.4187	0.1840	2.6036	45.2	ZnO	(002)	96-900-4182
	36.2420	0.1338	2.4767	62.5	ZnO	(101)	96-900-4182
	37.9481	0.2342	2.3691	35.9	SnO_2	(111)	96-900-9083
	51.7982	0.2174	1.7636	40.6	SnO_2	(211)	96-900-9083
	54.7421	0.1338	1.6755	66.9	SnO_2	(220)	96-900-9083
	56.5654	0.1505	1.6257	59.9	ZnO	(110)	96-900-4182
	57.8366	0.1840	1.5930	49.3	SnO_2	(002)	96-900-9083
	61.8846	0.2844	1.4981	32.6	SnO_2	(310)	96-900-9083
	64.7616	0.2175	1.4384	43.3	SnO_2	(112)	96-900-9083
	65.9493	0.2008	1.4153	47.2	SnO_2	(301)	96-900-9083
x=0.4	26.5905	0.1673	3.3496	48.8	SnO_2	(110)	96-900-9083
	31.7424	0.2007	2.8167	41.2	ZnO	(100)	96-900-4182
	33.8500	0.2007	2.6460	41.4	SnO_2	(101)	96-900-9083
	34.4355	0.2175	2.6023	38.2	ZnO	(002)	96-900-4182
	36.2253	0.1338	2.4778	62.5	ZnO	(101)	96-900-4182
	37.9481	0.2007	2.3691	41.9	SnO_2	(200)	96-900-9083
	51.7145	0.1840	1.7662	48.0	SnO_2	(211)	96-900-9083
	54.7087	0.1338	1.6764	66.8	SnO_2	(220)	96-900-9083
	61.8679	0.2174	1.4985	42.6	SnO_2	(310)	96-900-9083
	64.7449	0.2509	1.4387	37.5	SnO_2	(112)	96-900-9083
	65.9493	0.2175	1.4153	43.5	SnO_2	(301)	96-900-9083
x=0.6	26.5905	0.2007	3.3496	40.7	SnO_2	(110)	96-900-9083
	33.8500	0.1840	2.6460	45.1	SnO_2	(101)	96-900-9083
	37.9314	0.1840	2.3701	45.7	SnO_2	(200)	96-900-9083
	38.9685	0.1673	2.3094	50.4	SnO_2	(111)	96-900-9083
	51.7480	0.2174	1.7651	40.6	SnO_2	(211)	96-900-9083
	54.7589	0.2007	1.6750	44.6	SnO_2	(220)	96-900-9083
	57.8199	0.1840	1.5934	49.3	SnO_2	(002)	96-900-9083
	61.8679	0.2175	1.4985	42.6	SnO_2	(310)	96-900-9083
	64.7282	0.2175	1.4390	43.2	SnO_2	(112)	96-900-9083
	65.9493	0.1840	1.4153	51.5	SnO_2	(301)	96-900-9083
	71.2685	0.2341	1.3222	41.8	SnO_2	(202)	96-900-9083
	78.6953	0.2174	1.2149	47.3	SnO_2	(321)	96-900-9083
x=0.8	26.5570	0.2007	3.3537	40.7	SnO_2	(110)	96-900-9083
	33.8500	0.1840	2.6460	45.1	SnO_2	(101)	96-900-9083
	37.9481	0.1840	2.3691	45.7	SnO_2	(200)	96-900-9083
	39.0020	0.2007	2.3075	42.0	SnO_2	(111)	96-900-9083
	51.7982	0.2007	1.7636	44.0	SnO_2	(211)	96-900-9083
	54.7421	0.2175	1.6755	41.1	SnO_2	(220)	96-900-9083

	57.8701	0.2174	1.5921	41.8	SnO_2	(002)	96-900-9083
	61.8846	0.2174	1.4981	42.6	SnO_2	(310)	96-900-9083
	64.7449	0.2510	1.4387	37.5	SnO_2	(112)	96-900-9083
	65.9660	0.2509	1.4150	37.7	SnO_2	(301)	96-900-9083
	71.2685	0.2007	1.3222	48.7	SnO_2	(202)	96-900-9083
	78.6953	0.1506	1.2149	68.2	SnO_2	(321)	96-900-9083
	26.5905	0.0836	3.3496	97.6	SnO_2	(110)	96-900-9083
	33.8667	0.1505	2.6447	55.2	SnO_2	(101)	96-900-9083
	37.9314	0.2007	2.3701	41.9	SnO_2	(211)	96-900-9083
	51.7313	0.2175	1.7657	40.6	SnO_2	(310)	96-900-9083
	54.7254	0.1673	1.6759	53.5	SnO_2	(220)	96-900-9083
SnO_2	57.8032	0.1840	1.5938	49.3	SnO_2	(002)	96-900-9083
	61.8511	0.1673	1.4989	55.4	SnO_2	(310)	96-900-9083
	64.6780	0.1840	1.4400	51.1	SnO_2	(112)	96-900-9083
	65.8991	0.2007	1.4163	47.2	SnO_2	(301)	96-900-9083
	71.2350	0.1506	1.3227	64.9	SnO_2	(202)	96-900-9083
	78.6786	0.1673	1.2152	61.4	SnO_2	(321)	96-900-9083

The presence of many peaks in the XRD patterns of Fig.2 suggests that the composites are of high crystallinity and polycrystalline in nature. For samples of thin-film composites with x=0.8, a high crystalline phase was seen, as shown by sharp and intense diffraction peaks. It has previously been observed [24] that the XRD peaks shift towards higher angles as the composition (x) increases to 0.4, 0.6, and 1.0. This might be the result of intrinsic strain being released as composition increases. It is well known that crystalline defects cause micro strain lattice, such as gaps, stacking errors, interstitials, etc. As the composition ratio increased from x=0.2 to 0.4, the diffraction peaks consistently became sharper, indicating that the crystal size was growing. The Scherrer's formula can be used to determine the samples' crystal sizes, as listed in Table 2. The average crystalline size of $(ZnO)_{1-x}(SnO_2)_x$ nanocomposites showed a small decrease at x=0.6 and 0.8, which may be due to many reasons and need to be probed further. The X-ray pattern of the $(ZnO)_{0.6}$ $(SnO_2)_{0.4}$ composite thin film contains characteristic peaks of both the wurtzite and tetragonal structures. Thus, it can be concluded that the material $(ZnO)_{0.6}$ $(SnO_2)_{0.4}$ is a mixture of two phases and does not form a new compound.

3.2 Optical Analysis

The absorption coefficient for pure ZnO and other composites thin films as a function of wavelength within the range of 300–1100 nm, is depicted in Fig. 3. The absorption coefficient has large values $\alpha > 10^4$ at the short wavelengths, indicating a significant likelihood of authorized direct transmission. Then, as wavelength increased, α dropped. The absorption coefficient decreases with wavelength due to the donor output concentrations (local states) in the forbidden energy band and the valence band. It was shown that for all samples of $(ZnO)_{1-x}(SnO_2)_x$ composite films, the absorption coefficient rose as the photon energy increased. An electron in the absorption process is excited from lower to higher energy states by a photon of known energy, which corresponds to an absorption edge. The basic edge in crystalline materials is directly associated with the valence and conduction bands, or direct and indirect band gaps. The electrons and holes absorb a photon and a phonon in the different absorption processes. The necessary momentum is provided by the phonon, and the necessary energy is provided by the photon. Fundamental absorption, exciton absorption, and valence and acceptor absorption are the three factors that account for the absorption coefficient's fluctuation with photon

energy. Fundamental absorption and impurity-induced absorption are responsible for the peaks seen on the low energy side [25].

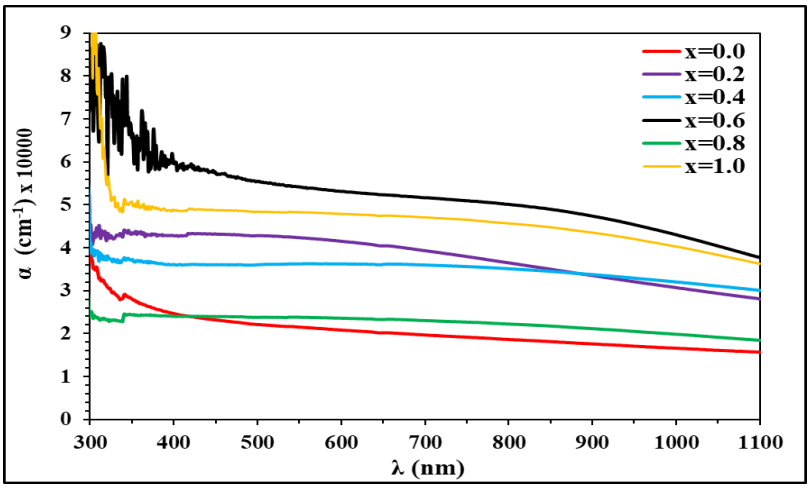

Figure 3: The absorption coefficient spectra of $(ZnO)_{1-x}(SnO_2)_x$ composites thin films.

The optical characteristics, such as band gap (E_g), and the transmission (T) spectra of $(ZnO)_{1-x}(SnO_2)_x$ composites thin films where x=0.2, 0.4, 0.6, 0.8, and 1.0 were measured and discussed. The transmittance fluctuation of $(ZnO)_{1-x}(SnO_2)_x$ composites thin films with wavelength produced at room temperature in the region of 300-1100 nm. Fig. 4 and Table 3 make it evident that the permeability value of $(ZnO)_{1-x}(SnO_2)_x$ composites thin films changed in a regular manner, i.e. decreases and increases by increasing tin oxide concentration. The reduction of the transmittance means that $(ZnO)_{1-x}(SnO_2)_x$ composites thin films absorb the incident radiation, which shifts the energy gap toward longer wavelength (lower energies). The rise in transmittance indicates that the increase of tin oxide concentration created $(ZnO)_{1-x}(SnO_2)_x$ composites thin film samples that are either reduced opacity or greater transparency toward the radiation that strikes it, which consequently shifting the absorption edge toward shorter wavelength (higher energies). This has to do with decreasing grain size because doing so raises the lattice parameters, which widens the energy gap [26].

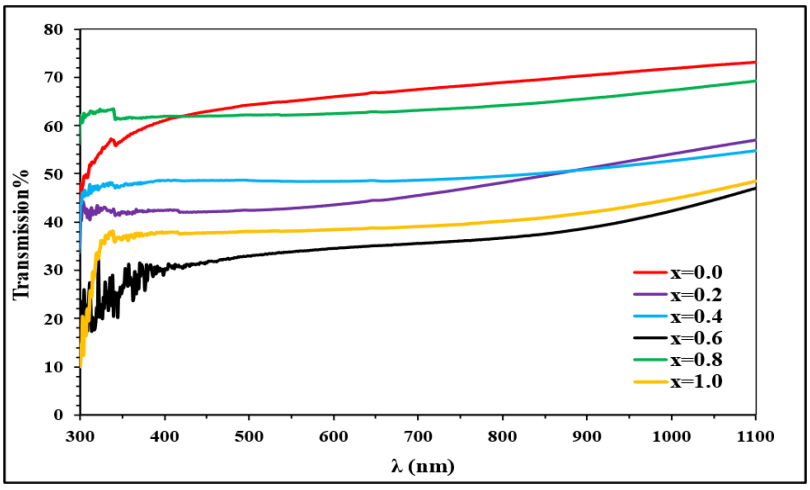

Figure 4: The transmittance spectra of $(ZnO)_{1-x}(SnO_2)_x$ composite thin films.

To assess the electrical properties of the $(ZnO)_{1-x}(SnO_2)_x$ composite thin films, the optical energy gap can be employed to determine the energy between the valence and

conduction lines [27]. This study demonstrated that all produced thin films have a direct energy gap, which can be determined by analyzing the absorption coefficient. The Tauc connection [28] was employed to calculate the direct optical energy gap (E_g). The point where the extended straight line of the $(\alpha h\nu)^2$ versus photon energy (hv) graph meets the (hv) axis gives us the value of Eg. The visual energy gap values of the $(ZnO)_{1-x}(SnO_2)_x$ composite were 3.30, 1.90, 3.4, 1.70, 2.60, and 3.70 eV for x= 0.0, 0.2, 0.4, 0.6, 0.8, and 1.0, respectively. Several variables affect semiconductor energy band gaps. The energy band gap may grow with decreasing particle size due to three-dimensional quantum size effects, disorder at grain boundaries, charged impurities, and defects. A lower optical energy gap was achieved by increasing the concentration of tin oxide. There are several possible explanations for the shrinking of the band gap. Adding oxygen vacancies to a material (through different synthesis techniques, doping, composites, etc.) narrows the band gap, which is linked to the material's photocatalytic activity, according to several research studies that detail the photocatalytic activity of materials. So, among other things, it's reasonable to assume that the band gap is narrowing in the manufactured composites thin films because the vacancy concentration is increasing. It is believed that nanocomposites of ZnO and SnO_2 have desirable photocatalytic characteristics [29]. The photocatalytic characteristics of ZnO/SnO_2 nanocomposites were recently presented by Hamrouni et al. [32], Kuzhalosai et al. [31], and Chiang et al. [30]. They noticed that the ZnO/SnO_2 nanocomposite is reusable and that its greater photocatalytic qualities are caused by heterojunctions between the two oxides compared to pure ZnO and SnO_2 nanoparticles. As is well known, altering the carrier concentration in degenerated semiconductors like ZnO and SnO_2 may raise or reduce the optical band gap. Consequently, when the concentration of SnO_2 or the concentration of carriers increases, so does the optical band gap value. It is seen from Fig. 5 that adding SnO_2 to ZnO at x= 0.2, 0.6 and 0.8 has reduced the band gap of $(ZnO)_{1-x}(SnO_2)_x$ composite films with respect to that of ZnO film while the addition of SnO_2 to ZnO at x= 0.4, and 1.0 have widened the band gap of $(ZnO)_{1-x}(SnO_2)_x$ composite films. Our results are similar to Young et al. findings [33], It shown that crystalline zinc-tin oxide (ZTO) thin films produced by sputtering displayed a direct optical band gap between 3.3 and 3.9 eV. They also came to the conclusion that the zinc-tin oxide thin films' structural and compositional differences might likely contribute to this wide band gap range. The shifting crystal size value seen from the x-ray diffraction data is the basis for our explanation of the energy gap's shrinking and widening. The narrowing of energy gap is related with growing of crystal size and hence, crystallinity enhancement while broadening of the energy gap is related with reduction of crystal size.

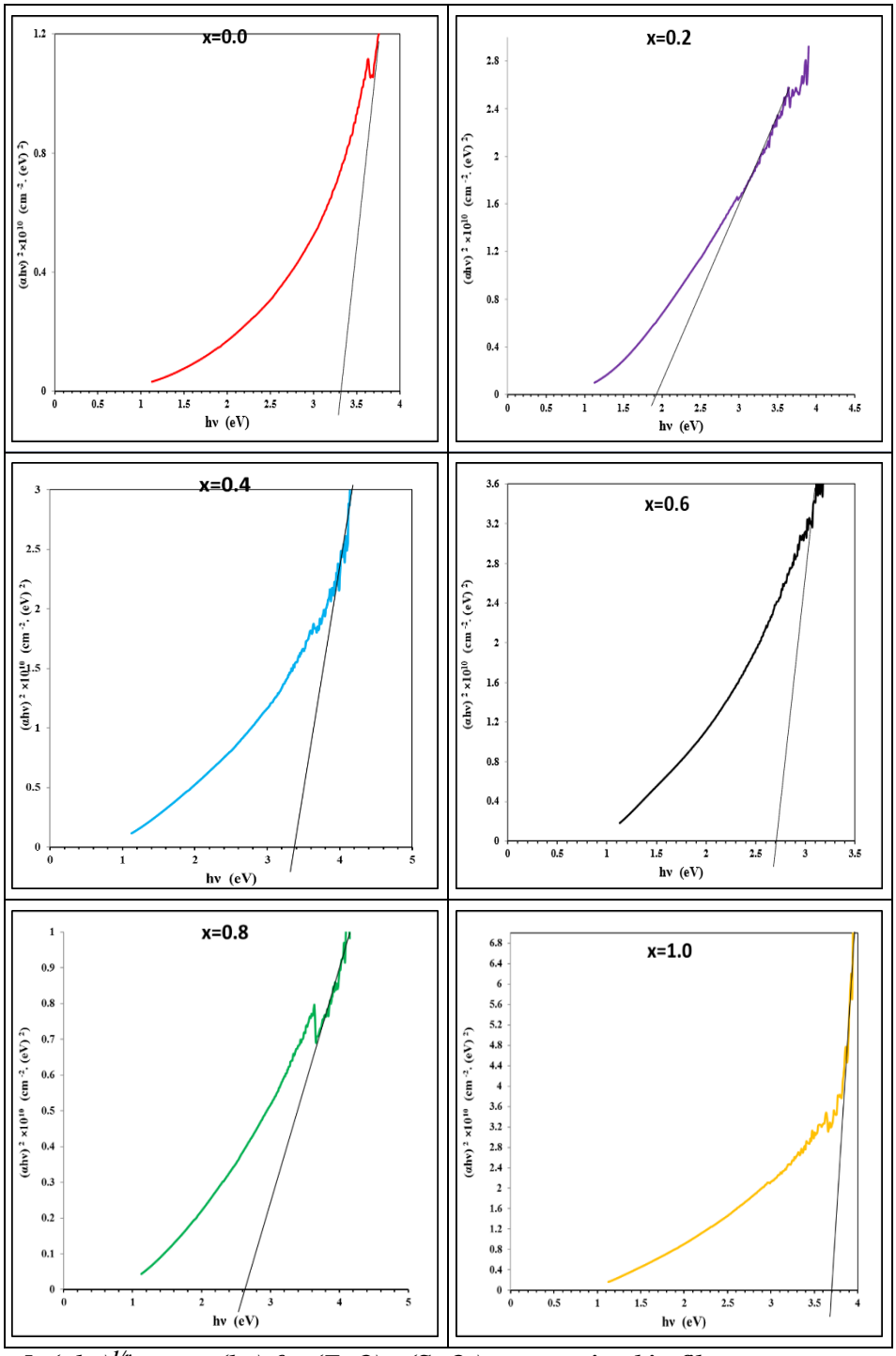

Figure 5: $(\alpha h\upsilon)^{1/r}$ versus $(h\upsilon)$ for $(ZnO)_{1-x}(SnO_2)_x$ composite thin films.

The refractive index (n) for (ZnO) and residual composites thin films samples with various metal oxide (SnO_2) concentrations as a function of wavelength were plotted as in Fig. 6. The figure and Table (3) show that n changes in a non-systematic sequence with the increase of tin oxide concentration. It was found that n values of tin oxide and all other composites exceeded that of pure zinc oxide, showing that the $(ZnO)_{1-x}(SnO_2)_x$ composite thin films became increasingly opaque to incident light as the amount of tin oxide increased [34-39].

Fig. 7 illustrates the extinction coefficient's (k) wavelength dependency. The data clearly shows that as λ increases, the values of k decrease and grow smaller in the region beyond the absorption edge. It should be noted that the values of zinc oxide are lower

than those of tin oxide (k) (at wavelength = 550 nm) for all composite samples. Eq. (5) [38] predicts that k increases, which can be linked to the increasing absorption coefficient.

Eqs. (8 and 9) were used to compute the real and imaginary components of the dielectric constant (ε_r and ε_i) of $(ZnO)_{1-x}(SnO_2)_x$ composite thin films formed at room temperature with varying tin oxide concentration. Based on the analysis of Figs. 8 and 9, which depict the dependence of the real (ε_r) and the imaginary part of the dielectric constant (ε_i) on λ, it can be concluded that the ε_i primarily depends on k values that are related to the variation of α, while the variation of ε_r primarily depends on the value of n^2 due to the smaller value of k comparison with n^2.

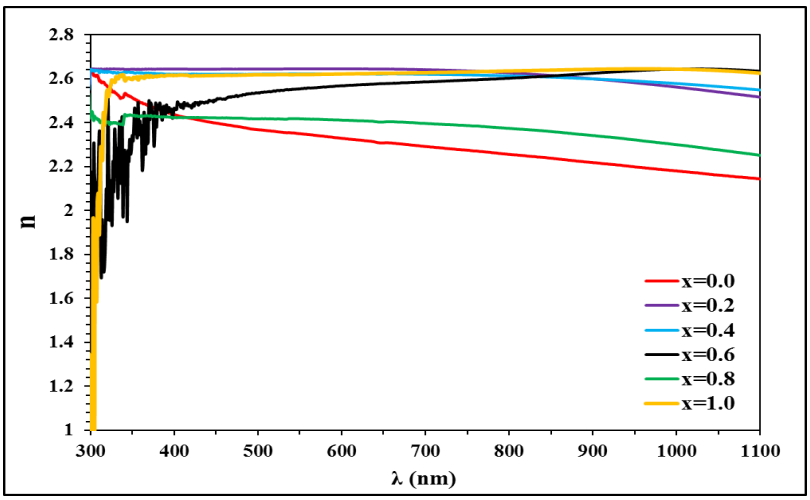

Figure 6: Variation of refractive index with wavelength of $(ZnO)_{1-x}(SnO_2)_x$ composites thin films.

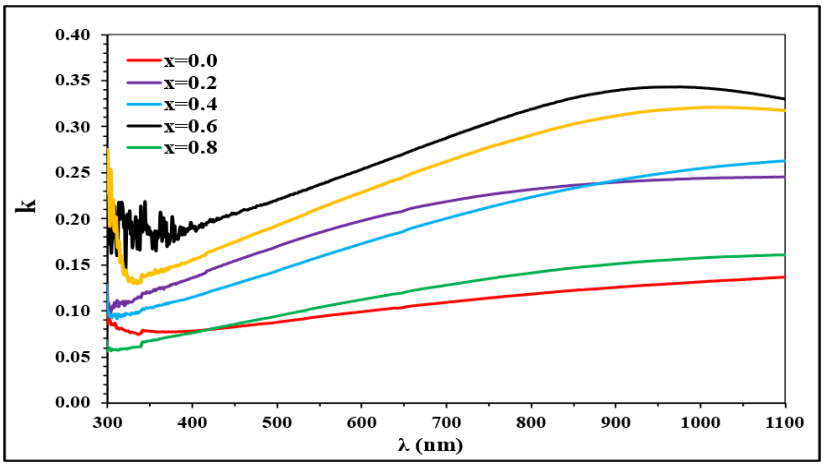

Figure 7: Extinction coefficient variation with wavelength of $(ZnO)_{1-x}(SnO_2)_x$ composites thin films.

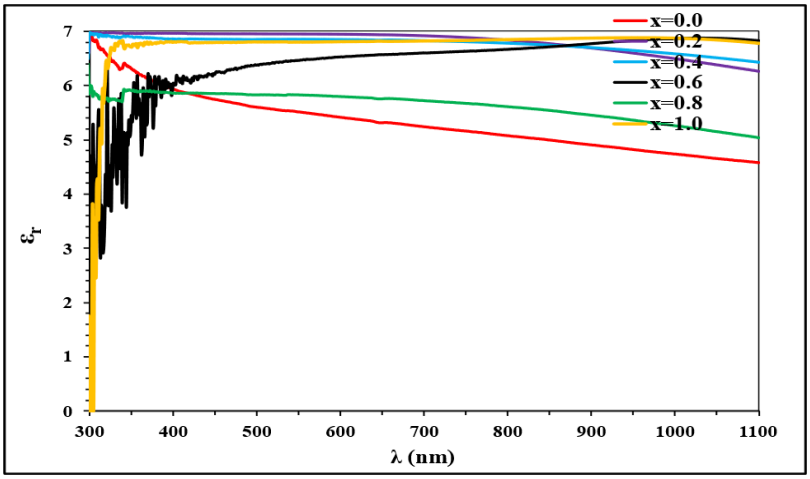

Figure 8: Real dielectric constant variation with wavelength of $(ZnO)_{1-x}(SnO_2)_x$ composites thin films.

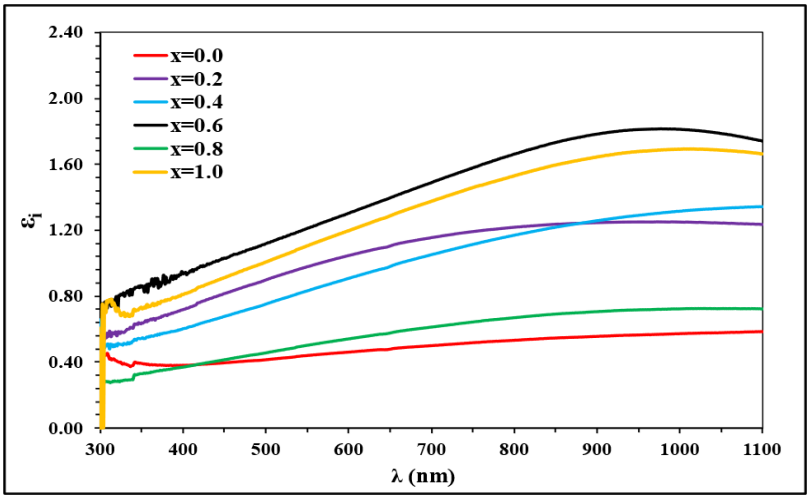

Figure 9: The imaginary dielectric constant's wavelength variation of $(ZnO)_{1-x}(SnO_2)_x$ composites thin films.

Table 3: The optical energy and optical constants of $(ZnO)_{1-x}(SnO_2)_x$ composites thin films at λ=550nm.

Sample	T%	α (cm^{-1})	k	n	ε_r	ε_i	E_g (eV)
0.0	65.13	21447	0.094	2.351	5.517	0.442	3.30
0.2	42.85	42375	0.186	2.643	6.953	0.981	1.90
0.4	48.50	36186	0.158	2.623	6.857	0.831	3.40
0.6	33.85	54167	0.237	2.553	6.462	1.211	1.70
0.8	62.17	23767	0.104	2.416	5.828	0.503	2.90
1.0	38.08	48277	0.211	2.617	6.806	1.107	3.70

3.3 Electrical property measurement

Hall measurements were performed to assess several factors, such as the kind of charge carrier, the charge carrier's Hall mobility (μH), and its carrier concentration (nH). The produced $(ZnO)_x(SnO_2)_{1-x}$ thin films that were coated on glass substrates are all measured by Hall in Table 4. This table makes clear that the pure sample had a negative Hall coefficient, or n-type charge carriers; in other words, the Hall voltage dropped as the current increased. This supports the findings of other studies [40-41]. It is clearly observed that the increase of tin oxide concentration did not change the type of conductance. The addition of tin oxide to the matrix oxide raised the concentration of the carrier nH of $(ZnO)_x(SnO_2)_{1-x}$ thin films, and as the tin oxide content grew, it varied non-

regularly. The reason for this is that as the crystal grows, more charge carriers move from the valence band to the conduction band; conversely, as the crystal gets smaller, more trapping centers form, which lowers the number of charge carriers moving from the valance band to the conduction band. Increased conductivity is caused by an increase in charge carriers, and this rise is most likely the consequence of the film's energy gap closing, which is consistent with the previous findings in this work. In contrast to nH, Hall mobility μH changed in the opposite way. It is evident that tin oxide addition significantly affects the trend of carrier concentration and mobility fluctuation.

Table 4: The measured parameters from Hall effect.

Sample	μ_H (cm^2/V.s)	σ $(ohm.cm)^{-1}$	R_H (cm^{-3}/C)	n_H $(cm)^{-3}$	Type
ZnO	4.53E+02	9.14E+00	4.96E+01	1.26E+17	n
$(ZnO)_{0.8}(SnO_2)_{0.2}$	1.21E+03	1.13E+02	1.06E+01	5.87E+17	n
$(ZnO)_{0.6}(SnO_2)_{0.4}$	1.91E+03	1.55E+01	1.23E+02	5.08E+16	n
$(ZnO)_{0.4}(SnO_2)_{0.6}$	2.03E+03	2.55E+01	7.96E+01	7.84E+16	n
$(ZnO)_{0.2}(SnO_2)_{0.8}$	1.90E+03	1.27E+01	1.49E+02	4.19E+16	n
SnO_2	2.01E+03	1.63E+01	1.23E+02	5.07E+16	n

4. Conclusions

In summary, the structural, chemical, and optical characteristics of $(ZnO)_{1-x}(SnO_2)_x$ composite thin films with various concentrations have been examined. The ratios of tin oxide to zinc oxide were established at 100:0, 80:20, 60:40, 40:60, 20:80, and 0:100 percent. It was noted that with compositional modification, the crystallinity of the composite films increased significantly and then decreased with higher concentrations of SnO_2. The average optical transmittance of the ZTO films throughout the visible spectrum 400-800 nm ranged from 65% to 33% as the SnO_2 concentration in the film increased. The optical band gap of the PLD films could be precisely adjusted by manipulating the SnO_2 ratio in the composite aggregate, ranging between the band gap of ZnO (E_g~3.3 eV) and SnO_2 (E_g~3.7 eV). The X-ray diffraction patterns of the $(ZnO)_{1-x}(SnO_2)_x$ composite films verified the development of mixed oxides instead of alloyed phases. The electrical conductivity of $(ZnO)_{1-x}(SnO_2)_x$ composite films significantly improved with the incorporation of SnO_2 at low concentrations x=0.2 and diminished at higher concentrations x=0.8 and 1.0 in comparison to pure ZnO films. The rise may be attributed to the increased carrier concentration and mobility resulting from the diffusion process, along with reduced grain-boundary scattering. The current study has shown that $(ZnO)_{1-x}(SnO_2)_x$ composite films may serve as viable candidates for optoelectronic applications, including solar cells and touch panel controls, due to their superior structural, optical, and electrical features.

Conflict of Interest

The authors declare no conflict of interest.

References

1. S.M. Pawar, B.S. Pawar, J.H. Kim, O.S. Joo, and C.D. Lokhande, Current Applied Physics, **11**, 117(2011).https://doi.org/10.1063/1.4922732.
2. L. Wen, M. Kumar, B. B. Sahu, S. B. Jin, C. Sawangrat, K. Leksakul and J. G. Han, Surface and Coatings Technology. **284**, 85 (2015). https://doi.org/10.1016/j.surfcoat.2015.06.084.
3. B.B. Sahu, S.B. Jin, P.J. Xiang, J.B. Kim, and J.G. Han, Journal of Applied Physics, 123, 134 (2018). https://doi.org/10.1002/ppap.201500094.
4. W. Yang, B. Cai, K. J. Lachowski, Q. Yin, J. J. De Yoreo, L. D. Pozzo and C. L. Chen, The Journal of Physical Chemistry Letters, **14**, 9732(2023). https://doi.org/10.1021/acs.jpclett.3c01882.
5. Q. Dawei, L. Xie, M. Yang, X. Meng, Y.-Q.Yi, Y. Hao, W. Su, L. Xu, Y. Gai, and Z. Cui, ACS Applied Electronic Materials, **4**, 1875 (2022). https://doi.org/10.1021/acsaelm.2c00088.

6. D. Kim and J. Y. Leem, RSC advances. **11**, 876 (2021). DOI: https://doi.org/10.1039/D0RA9869H.
7. J. Rodrigues, C. Becker, N. B. Sedrine, M. Kamp, L. Kienle, R. Adelung and T. Monteiro, Journal of Materials Chemistry C. **9**, 7014 (2021). https://doi.org/10.1039/D1TC00099C.
8. G. W. Hsieh, S. R. Ling, F. T. Hung, P. H. Kao and J. B. Liu. Nanoscale. **13**, 6076 (2021). https://doi.org/10.1039/D0NR06743A.
9. N. Cheng, L. Zhang, J. J. Kim and T. L. Andrew. Journal of Materials Chemistry C. **5**, 5787 (2017). https://doi.org/10.1039/C7TC00293A.

J. Ma, S. Yamashita, Y. Muroya, Y. Katsumura and M. Mostafavi, Physical Chemistry Chemical Physics. **17**, 22934 (2015). https://doi.org/10.1039/c5cp04293c.

11. A. Büter, G. Maschkowitz, M. Baum, Y. K. Mishra, L. Siebert, R. Adelung and H. Fickenscher. International Journal of Molecular Sciences, **24**, 3444 (2023). https://doi.org/10.3390/ijms24043444.
12. M. González-Garnica, A. Galdámez-Martínez, F. Malagón, C. D. Ramos, G. Santana, R. Abolhassani, and A. Dutt. Sensors and Actuators B: Chemical. **337**, 129765 (2021). https://doi.org/10.1016/j.snb.2021.129765.
13. Y. K. Mishra, G. Modi, V. Cretu, V. Postica, O. Lupan, T. Reimer, and R.Adelung. ACS applied materials & interfaces, **7**, 14303 (2015). https://doi.org/10.1021/acsami.5b02816.
14. I. Paulowicz, V. Hrkac, S. Kaps, V. Cretu, O. Lupan, T. Braniste and Y. K. Mishra. Advanced Electronic Materials. **1**, 1500081 (2015). https://doi.org/10.1002/aelm.201500081.
15. O. Lupan, T. Braniste, M. Deng, L. Ghimpu, I. Paulowicz, Y. K. Mishra, and I. Tiginyanu. Sensors and Actuators B: Chemical. **221**, 544 (2015). https://doi.org/10.1016/j.snb.2015.06.112.
16. H. S. Das, S. Mishra, M. K. Dash, P. Kumar, S. K. Maity, D. Khatua and G. Roymahapatra. ES Materials & Manufacturing. **22**, 841 (2023). https://doi.org/10.30919/esmm5f841.
17. T. B. Quan, N. K. Binh, V. T. N. Thuy, N. H. Dang and P. T. K. Hang. Tạp chí Khoa học Đại học Đồng Tháp. **13**, 113 (2024). https://doi.org/10.52714/dthu.13.5.2024.1295.
18. C. R. Conti III, G. Quiroz-Delfi, J. S. Schwarck, B. Chen and G. F. Strouse. The Journal of Physical Chemistry C. **124**, 28220 (2020). https://doi.org/10.1021/acs.jpcc.0c09448.
19. Y. Wang, B. Li, C. Jiang, Y. Fang, P. Bai and Y. Wang. The Journal of Physical Chemistry C. **125**, 16753 (2021). https://doi.org/10.1021/acs.jpcc.1c04138.
20. T. Ohsawa, N. Yamada, A. Kumatani, Y. Takagi, T. Suzuki, R. Shimizu and T. Hitosugi. ACS Applied Electronic Materials. **2**, 517 (2020). https://doi.org/10.1021/acsaelm.9b00751.
21. T. Minami, H. Sonohara, S. T. S. Takata and H. S. H. Sato. Japanese journal of applied physics. **33**, L1693 (1994). https://doi.org/10.1143/JJAP.33.L1693.
22. A. A. Al-Bayati and H. F. Ali, Iraqi Journal of Physics. **23**, 68 (2025). https://doi.org/10.30723/ijp.v23i1.1334.
23. S. M. Hanfoosh and N. K. Hassan. Iraqi Journal of Science. **60**, 2009 (2019). https://doi.org/10.24996/ijs.2019.60.9.14.
24. O. Lupan, T. Pauporte, L. Chow, B. Viana, F. Pelle, L.K. Ono, B.R.Cuenya and H. Heinrich, Applied Surface Science, **256,** 1895 (2010). https://doi.org/10.1016/j.apsusc.2009.10.032.
25. H. H. Abbas, B. A. Hasan, Iraqi Journal of Science, **63**, 1526 (2022). https://doi.org/10.24996/ijs.2022.63.4.13.
26. M. A. Abood, B. A. Hasan, Iraqi Journal of Science, **64**, 1675 (2023). https://doi.org/10.24996/ijs.2023.64.4.10.
27. S. Sönmezoğlu, G. Çankaya, and N. Serin, Materials Science and Technology, **27**, 251 (2012). https://doi.org/10.1179/1753555712Y.0000000008.
28. I. M. Ibrahim, A. S. Mohammed and A. Ramizy, Journal of Ovonic Research, **14**, 17, (2018).
29. K.G. Ewsuk, D.T. Ellerby, C.B. DiAntonio, J. Am. Ceram. Soc. **89**, (2006).
30. Y.J. Chiang, C.C. Lin, Powder technology. **246**, 137 (2013). https://doi.org/10.1016/j.powtec.2013.04.033.
31. V. Kuzhalosai, B. Subash, A. Senthilraja, P. Dhatshanamurthi, M.Shanthi, Spectrochim. Acta A Mol. Biomol. Spectrosc. **115**, 876 (2013).
32. A. Hamrounia, N. Moussaa, F. Parrinob, A.D. Paolab, A. Houasa,L. Palmisano Journal of Molecular Catalysis A: Chemical. **390**, 133 (2014). https://doi.org/10.1016/j.molcata.2014.03.018.
33. D. L. Young, H. Moutinho, Y. Yan and T. J. Coutts. *Journal of applied physics*. **92**, 310 (2002). https://doi.org/10.1063/1.1483104.
34. B.A. Hasan, I.J.S.N., **8**, 1 (2017).
35. G. H Mohammed, H. J. Abdul Karim, AIP Conference Proceedings. **2372**, (2021). https://doi.org/10.1063/5.0068747.
36. H. J. Abdul Karim, and G. H Mohammed, Solid State Technology, **63**, 5266 (2020).
37. A. K. Jazmati and B. Abdallah, Materials Research, **21**, 20170821 (2018). https://doi.org/10.1590/1980-5373-MR-2017-0821.
38. H. J. Abdul Karim, B. F Al-Azzawi, M. E Hammadi and G. H Mohammed, Journal of Optics, **53**, 110 (2024). https://doi.org/10.1007/s12596-024-01944-5 .

39. B. A. Hasan, D. A. Umran and M. A. K. Mankoshi. In Journal of Physics: Conference Series. **1032**, 012020. IOP Publishing, (2018). https://doi.org/10.1088/1742-6596/1032/1/012020 .
40. S. Jäger, B. Szyszka, J. Szczyrbowski, and G. Bräuer. Surface and coatings technology. **98**, 1304 (1998). https://doi.org/10.1016/S0257-8972(97)00145-X.
41. J. Owen, M.S. Son, K.-H. Yoo, B.D. Ahn and S.Y. Lee. Appl. Phys. Lett. **90,** 033512 (2007). https://doi.org/10.1063/1.2432951.

دور اوكسيد الخارصين على الخواص التركيبية والبصرية والكهربائية لاغشية أكسيد الزنك وثاني أكسيد القصدير الرقيقة المحضرة بالترسيب بالليزر النبضي

ليث ابراهيم خليل[1] ,بشرى عباس حسن[1]
[1] قسم الفيزياء، كلية العلوم، جامعة بغداد، بغداد، العراق

الخلاصة
يتناول هذا البحث دراسة تأثير تركيز المكونات لمتراكبات الاغشية الرقيقة $(ZnO)_{1-x}(SnO_2)_x$ المحضرة بالترسيب بالليزر النبضي على خواصها التركيبية والبصرية والكهربائية. أجريت الدراسة التركيبية لمتراكبات الأغشية الرقيقة $(ZnO)_{1-x}(SnO_2)_x$ باستخدام تقنية XRD. تم فحص الخصائص البصرية بواسطة التحليل الطيفي للأشعة تحت الحمراء UV-Vis. أوضح التحليل البنيوي أن كل مركب من الأغشية الرقيقة المحضرة كان عبارة عن طور متعدد البلورات وورزيت سداسي ورباعي الأضلاع لـ ZnO وSnO_2 النقي ومختلط من كلا الطورين لـ x=0.2 و0.4 بينما كان طور SnO_2 هو السائد لـ x=0.6,0.8. وقد لوحظ الارتفاع في حجم البلورات في الأغشية الرقيقة المركبة $(ZnO)_{1-x}(SnO_2)_x$ عند x=0.4 و1.0. أظهرت فجوة النطاق في بصريات المركبات $(ZnO)_{1-x}(SnO_2)_x$ اختلافاً في السلوك بزيادة تركيز أكسيد القصدير. وكان متوسط النفاذ البصري في المدى (33-65)% في المنطقة المرئية. تم الحصول على الحد الأقصى للتوصيل الكهربائي $1.13\times10^{2}(\Omega cm)^{-1}$ في الغشاء $(ZnO)_{0.8}(SnO_2)_{0.2}$. تشير نتائجنا إلى أن متراكبات الاغشية $(ZnO)_{1-x}(SnO_2)_x$ ذات الخصائص الكهربائية والبصرية المحسنة يمكن أن تجد استخدامًا محتملاً في الخلايا الشمسية ذات الأغشية الرقيقة أو لوحات التحكم باللمس.

الكلمات المفتاحيه: غشاء رقيق. ثاني أكسيد القصدير (SnO_2)، أكسيد الزنك (ZnO)، PLD. الخواص البصرية والهيكلية.